ACS APPLIED MATERIALS & INTERFACES

Research Article

www.acsami.org

Microstructural Evolution of Nanocrystalline Diamond Films Due to $CH_4/Ar/H_2$ Plasma Post-Treatment Process

Sheng-Chang Lin,[†] Chien-Jui Yeh,[†] Divinah Manoharan,[‡] Keh-Chyang Leou,[†] and I-Nan Lin*[,‡]

[†]Department of Engineering and System Science, National Tsing Hua University, Hsinchu, Taiwan 300, R.O.C.

[‡]Department of Physics, Tamkang University, Tamsui, Taiwan 251, R.O.C.

ABSTRACT: Plasma post-treatment process was observed to markedly enhance the electron field emission (EFE) properties of ultrananocrystalline diamond (UNCD) films. TEM examinations reveal that the prime factor which improves the EFE properties of these films is the coalescence of ultrasmall diamond grains (~5 nm) forming large diamond grains about hundreds of nanometers accompanied by the formation of nanographitic clusters along the grain boundaries due to the plasma post-treatment process. OES studies reveal the presence of large proportion of atomic hydrogen and C_2 (or CH) species, which are the main ingredients that altered the granular structure of the UNCD films. In the post-treatment process, the plasma interacts with the diamond films by a diffusion process. The recrystallization of diamond grains started at the surface region of the material, and the interaction zone increased with the post-treatment period. The entire diamond film can be converted into a nanocrystalline granular structure when post-treated for a sufficient length of time.

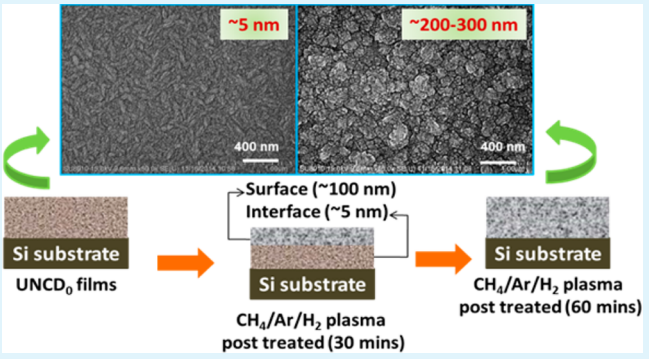

KEYWORDS: *post-treatment, diamond films, nanocrystalline, microstructure, electron field emission*

INTRODUCTION

Diamond field emitters strongly compete with cold cathode materials for flat panel displays.[1−4] Diamond films also have attracted significant attention in vacuum microelectronics due to their low electron affinity for electron emission, strong bonding structure, extreme hardness to withstand ion bombardment, and good thermal and electrical conductivities to handle high currents.[5−7] However, in CH_4/H_2 plasma-grown microcrystalline diamond (MCD) films, the large diamond grains (>1 μm) with large electronic band gap of 5.1 eV obstructs the electron field emission (EFE) behavior of the materials due to a lack of the electrons required for field emission.[8,9] Nanocrystalline diamond (NCD) films with nanosized diamond grains (~hundreds of nanometers) are expected to conduct electrons better than microcrystalline diamond (MCD) films due to the abundance of grain boundaries. However, the grain boundaries in NCD films are usually very sharp, showing highly insulating characteristics, which limit the EFE behavior of the materials. Moreover, the conductivity of the NCD films varies with the plasma chemistry used for achieving small grain size, and the reported results are thus inconsistent.[10−12]

The bias-enhanced growth (beg) process has been proven to be a very effective growth process to induce the formation of the nanographitic phase along the grain boundaries of diamond films,[13−15] which improves the electrical properties of the NCD films. The negative bias voltage applied while using the CH_4/H_2 plasma in the microwave plasma-enhanced chemical vapor deposition (MPECVD) sequences not only facilitates the fast growth of diamond films, but also converts the amorphous carbon (*a*-C) phases into nanographite phases, as well as efficiently reduces the grain size. Even for a low-cost substrate, the use of negative bias can lead to epitaxial growth of diamond films with increased nucleation density.[16,17] The formation of sp^2 bonded graphitic phases at the grain boundaries, which create conduction channels for the electrons to be transported, accounts for the improved EFE properties.[18]

In the present work, a novel approach for enhancing the EFE properties of NCD films is being adopted, wherein diamond films with ultrasmall grains (~5 nm) using CH_4/Ar plasma were first grown, followed by post-treatment in $CH_4/Ar/H_2$ plasma to convert the granular structure of the diamond films into a nanocrystalline one (~hundreds of nm). The evolution of the granular structure of the diamond films resulting from the plasma post-treatment process was systematically examined using transmission electron microscopy (TEM). The probable mechanism for the improvement of the EFE properties of the NCD films due to these post-treatment processes is discussed in detail.

EXPERIMENTAL SECTION

The diamond films with ultrasmall diamond grains, i.e., the ultrananocrystalline (UNCD) films, were first grown on Si for

Received: July 7, 2015
Accepted: September 15, 2015
Published: September 15, 2015

DOI: 10.1021/acsami.5b06074
ACS Appl. Mater. Interfaces 2015, 7, 21844−21851

investigating the effect of the post-treatment process on the evolution of microstructure of diamond films. The Si substrates were preseeded by ultrasonication in methanol solution containing nanosized diamond powders (~5 nm) and Ti powders (~32.5 nm). The UNCD films were grown on the Si using an MPE-CVD process (2.45 GHz, IPLAS-CYRANNUS) in a CH_4 (2%)/Ar (98%) plasma with a microwave power of 1200 W for 60 min, with a pressure and total flow rate of 197 mbar (150 Torr) and 200 sccm (standard cubic centimeter), respectively. The UNCD films were grown for 120 min to reach a thickness ~800 nm. Subsequently, the UNCD/Si films were post-treated in a CH_4 (2%)/Ar (48%)/H_2 (50%) plasma, which was excited by 1300 W microwave power in 86 mbar (65 Torr) chamber pressure, with −300 V negative bias voltage applied on Si for different period of time, say 30 and 60 min, to obtain diamond films of submicron grains, which are designated as NCD_{1b} and NCD_{2b} films, respectively.

The surface morphology and the crystalline quality of the diamond films were characterized using Scanning electron microscopy (SEM; Jeol JSM-6500) and Raman spectroscopy (λ: 325 nm, Lab Raman HR800, Jobin Yvon), respectively. The detailed microstructure and bonding structure of the samples were examined using Transmission electron microscopy (TEM, Jeol 2100F) and electron energy loss spectroscopy in TEM (EELS, Gatan Enfina), respectively. The EFE properties of the diamond films were measured using a tunable parallel plate setup, in which the anode is a Cu-rod around 3 mm in diameter, and the cathode-to-anode distance was controlled using a micrometer. The current−voltage (I−V) characteristics are acquired using an electrometer (Keithley 2410) under pressure below 1.3×10^{-6} mbar (10^{-6} Torr). The EFE parameters were extracted from the obtained I−V curves by using a Fowler−Nordheim (F−N) equation.[19] The turn-on field (E_0) was designated as the point of interception of the straight lines extrapolated from the low and high-field segments of the F−N plots, namely, ln (J_e/E^2) versus $1/E$ plots, where J_e is the EFE current density, and E is the applied field. The optical emission spectra of the plasma used for growing UNCD films and those used for plasma post-treatment process were acquired for the purpose of investigating the mechanism by which these processes modified the granular structure of the films.

RESULTS AND DISCUSSION

Figure 1 shows the evolution of SEM surface morphology of UNCD films due to the $CH_4/Ar/H_2$ post-treatment process (under −300 V bias voltage). The $UNCD_0$ films possess granular structure with ultrasmall grains (~5 nm) (Figure 1a). $CH_4/Ar/H_2$ plasma post-treatment process for 30 min induced the coalescence of the ultrasmall diamond grains, forming diamond aggregates about 100 nm in size for NCD_{1b} samples (Figure 1b). The sizes of diamond aggregates are slightly larger for NCD_{2b} samples, which were post-treated for 60 min (Figure 1c). The NCD_{2b} samples exhibit cauliflower-like morphology.

The Raman spectrum shown as curve I in Figure 2 indicates that the $UNCD_0$ films contain broad Raman resonance peaks due to the smaller size of diamond grains. The presence of a D-band (1350 cm^{-1}) and a G-band (1580 cm^{-1}) corresponding to sp^2-bonded carbon represents the disordered carbon and graphitic phase.[20,21] The υ_1-band (1140 cm^{-1}) and υ_3-band (1480 cm^{-1}) represents the transpolyacetylene (tPA) phase present at grain boundaries.[22,23] Moreover, there exists a sharp peak at 1332 cm^{-1} (D′-band), which corresponds to large grain diamond, the sp^3-bonded carbon. This figure shows that the $UNCD_0$ films consist of some large diamond grains coexisting with ultrasmall diamond grains. Curves II and III in Figure 2 show that the characteristics of the Raman spectra of the $CH_4/Ar/H_2$ plasma post-treated NCD samples are similar to those of $UNCD_0$ films, except that the intensity of diamond peak (D′-band at 1332 cm^{-1}) increases with post-treatment time. The increase in D′-band peak intensity signifies that the diamond

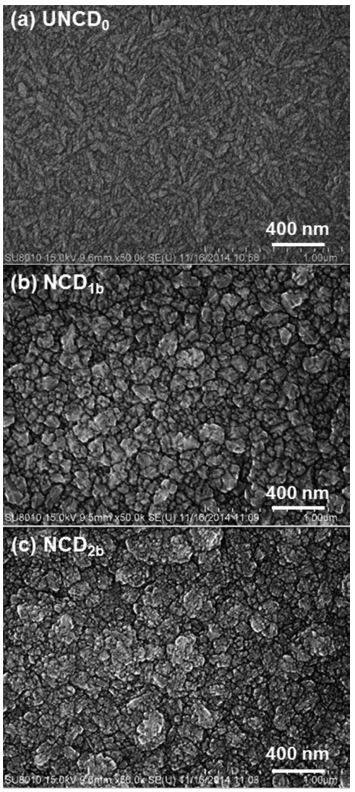

Figure 1. SEM micrographs of (a) $UNCD_0$ films, (b) UNCD films post-treated in $CH_4/Ar/H_2$ plasma for 30 min, NCD_{1b}, and (c) 60 min, NCD_{2b}.

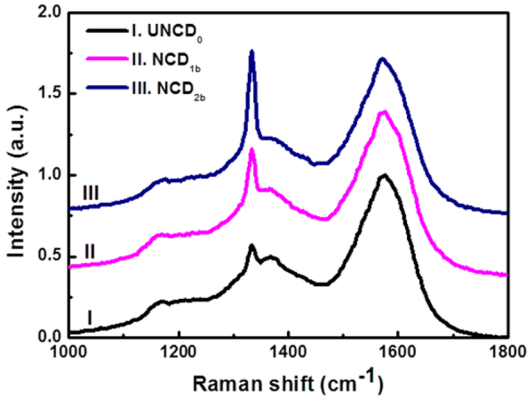

Figure 2. Raman spectra of (I) $UNCD_0$ films (II) UNCD films post-treated in $CH_4/Ar/H_2$ plasma for 30 min, NCD_{1b}, and (III) 60 min, NCD_{2b}.

grains grew larger, and the population of large diamond grains increases due to the plasma post-treatment processes. Moreover, there exists a shoulder peak corresponding to graphitic phase, (G'-band at 1600 cm^{-1}, curve I), which indicates the formation of nanographitic clusters.[23] Restating, the post-treatment process increases the proportion of large diamond grains. Such a characteristic is in accord with SEM observations.

A more intriguing observation is that the plasma post-treatment process markedly improved the EFE properties of diamond films. Figure 3a (curve I) shows that the EFE process of $UNCD_0$ films can be turned on at $((E_0)_0) = 38.2$ V/μm with EFE current density of $(J_e)_0 = 0.66$ mA/cm^2 at an applied field of 64.8 V/μm. The turn-on field for EFE process decreases

DOI: 10.1021/acsami.5b06074
ACS Appl. Mater. Interfaces 2015, 7, 21844−21851

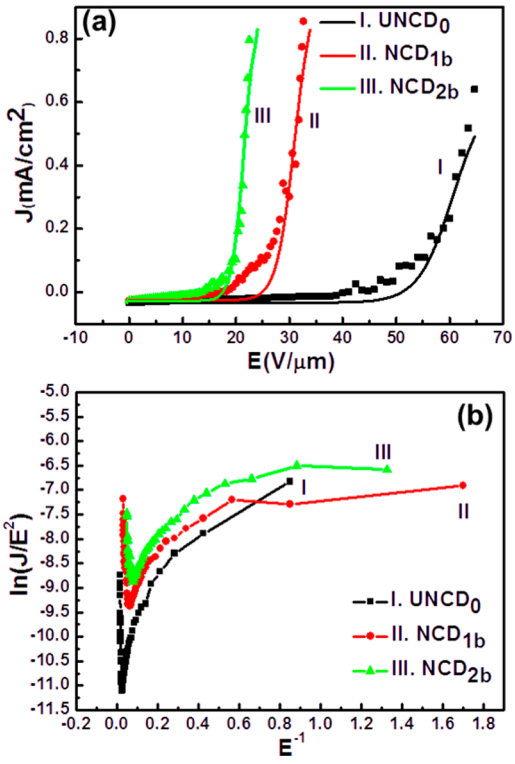

Figure 3. (a) EFE properties and (b) the corresponding F–N plots of (I) $UNCD_0$ films (II) UNCD films post-treated in $CH_4/Ar/H_2$ plasma for 30 min, NCD_{1b}, and (III) 60 min, NCD_{2b}.

monotonously with the period of $CH_4/Ar/H_2$ plasma post-treatment process. The EFE process of NCD_{2b} films can be turned on at $(E_0)_{2N}$ = 13.6 V/μm, achieving an EFE current density of $(J_e)_{2b}$ = 0.8 mA/cm^2 at an applied field of 21.5 V/μm. The EFE parameters, including E_0 and J_e, were extracted from the J_e–E curves and are summarized in Table 1. It is surprising

Table 1. Electron Field Emission Parameters, Turn-on Field (E_0) and EFE Current Density (J_e) of UNCD Films and those Post-Treated in $CH_4/Ar/H_2$ Plasma with and without −300 V Bias Voltage

samples	post-treatment condition	E_0 (V/μm)	J_e (mA/cm^2)
pristine		38.2	0.66 @ 64.8 V/μm
NCD_{1b}	−300 V (30 min)	16.5	0.87 @ 32.0 V/μm
NCD_{2b}	−300 V (60 min)	13.6	0.80 @ 21.5 V/μm

to observe that the EFE properties of diamond films were improve even when the plasma post-treated UNCD films possess markedly larger diamond grains compared to those of the $UNCD_0$ films.

The SEM surface morphology and Raman bonding structure cannot adequately explain how the EFE behavior of UNCD samples was improved due to the $CH_4/Ar/H_2$ plasma post-treatment process. Apparently, understanding of the modification of the microstructure of the materials due to these processes is necessary to account for the causes that alter the EFE behavior of the samples. Figure 4 shows the TEM micrographs of the $UNCD_0$ films. It should be noted that in the preparation of TEM foil, the samples can be either ion-milled from the Si-side, resulting in a thin foil which mainly contains the materials near the surface region of the films (designated as "surface"), or ion-milled from diamond- and Si-sides simultaneously, resulting in a thin foil which mainly contains the materials near the Si-substrate (designated as "interface"). Figure 4, parts a_I and b_I, shows the bright field (BF) TEM micrographs of the surface and interface regions of $UNCD_0$ films, respectively. These micrographs reveal that the microstructure of the interface region is the same as that in the surface region, i.e., both regions contain some diamond aggregates, ∼30–80 nm in size (indicated by arrows) scarcely distributed among the matrix of ultrasmall diamond grains. Selected area electron diffraction (SAED) patterns shown as insets in Figure 4, parts a_I and b_I, reveal the presence of smooth diffraction rings corresponding to $(111)_D$, $(220)_D$, and $(311)_D$ of diamond lattice planes, confirming that both surface and interface regions of the samples are predominantly diamond. Presumably, the areas showing no contrast are also diamond grains, but they are oriented away from the zone axis, diffracting electrons weakly. The continuous diffraction rings indicate that the diamond grains are ultrasmall in size and are randomly oriented. There exists a prominent central diffuse ring, indicating the presence of sp^2-bonded carbon in these samples. The granular structure of the $UNCD_0$ films is better illustrated by the composed dark field (c-DF) TEM micrographs, which are the superposition of TEM (DF) images acquired using different portions of the ⟨111⟩ diffraction ring, as indicated by circles in the insets in Figure 4, parts a_{II} and b_{II}, for surface and interface regions of $UNCD_0$ films, respectively. These micrographs reconfirm that the microstructures of the surface and interface regions are very alike, i.e., both of them contain large diamond aggregates evenly dispersed in a matrix of ultrasmall diamond grains. Restated, the $UNCD_0$ films possess very uniform granular structure throughout the thickness of the sample.

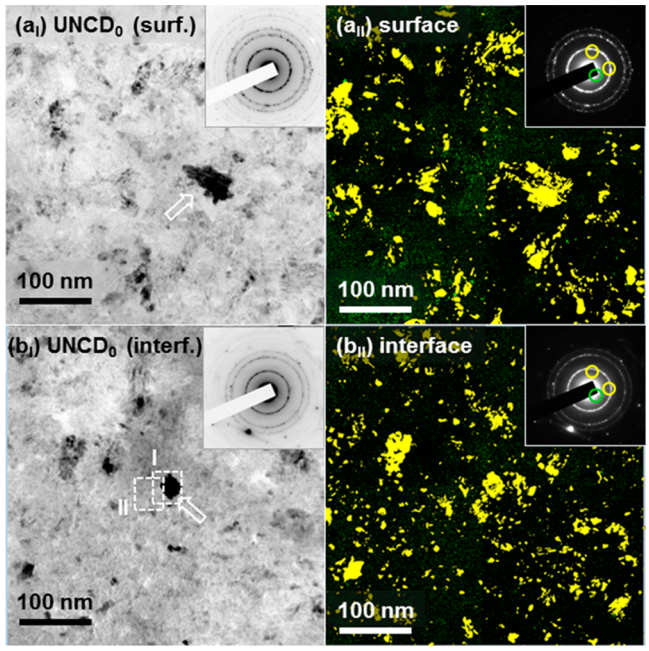

Figure 4. (a_I, b_I) Bright field and (a_{II}, b_{II}) composed dark field TEM micrographs of $UNCD_0$ films, where a_I and a_{II} are for the surface region and b_I and b_{II} are for the interface region of the films. The inset shows the corresponding selected area diffraction patterns.

The phase constituents of diamond films are best illustrated by the selected area EELS spectra. The core-loss and plasmon-loss EELS spectra are shown in Figure 5, parts a and b,

DOI: 10.1021/acsami.5b06074
ACS Appl. Mater. Interfaces 2015, 7, 21844–21851

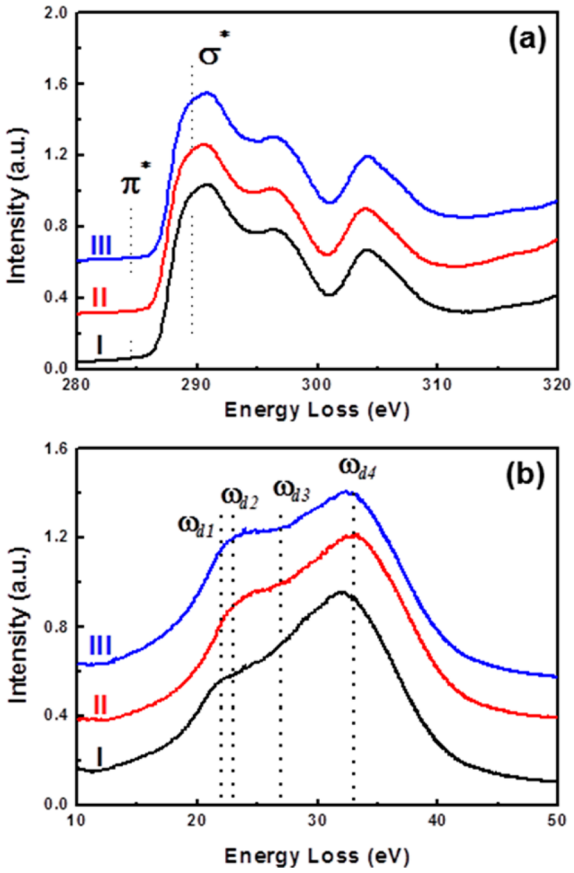

Figure 5. Selected area (a) core-loss EELS and (b) plasmon-loss EELS corresponding to the (I) representative regions (surface or interface regions) of $UNCD_0$, (II) surface, and (III) interface region of 60 min plasma post-treated (NCD_{2b}) films.

respectively. Notably, while the core-loss EELS spectrum shows the general feature of the diamond as the σ^*-band near 289.5 eV and the sp^2-bonded carbon (the graphite or a-C phase) as the π^*-band near 284.5 eV, it is the plasmon-loss EELS spectrum, which can unambiguously differentiate the a-C and the graphite phases in the sp^2-bonded carbon.[24−27]

In the plasmon-loss EELS spectrum, the a-C phase exhibits a peak near 22 eV (ω_{d1}-band), whereas the graphite phase shows a peak near 27 eV (ω_{d3}-band).[24−27] In contrast, the diamond phase exhibits a peak at 33 eV (ω_{d4}-band) corresponding to bulk plasmon with a shoulder at 23 eV (ω_{d2}-band) corresponding to the surface plasmon, and the ω_{d2}/ω_{d4} peak ratio is $\sim 1/\sqrt{2}$.[24−27] Curve I in Figure 5a shows that the core-loss EELS spectra of $UNCD_0$ films exhibit an abrupt rise near 289.5 eV (σ^*-band) and a deep valley near 302 eV, regardless of whether it is of the surface or interface regions. These bands are signatures of sp^3-bonded carbon, indicating that both the surface and interface regions of the $UNCD_0$ films are predominately diamond. There is an insignificantly small proportion of sp^2-bonded carbon. Moreover, curve I in Figure 5b shows the plasmon-loss EELS spectrum corresponding to surface and interface regions of $UNCD_0$ films, which exhibit the characteristic spectrum of diamond materials, i.e., they all show a resonant peak at 33 eV (ω_{d4}-band) with a shoulder at 23 eV (ω_{d2}-band).

However, more detail analysis reveals a subtle difference of these EELS spectra from those of typical diamond materials. The peak intensity ratio, ω_{d2}/ω_{d4}, in curve I (Figure 5b) is slightly larger than $1/\sqrt{2}$. The implication of such a deviation from $1/\sqrt{2}$ ratio is that these UNCD films contain small amounts of amorphous carbon or the nanographite phase. The existence of a small amount of amorphous carbon is also inferred from the presence of a ω_{d1}-band at 22 eV and that of the nanographite phase from the ω_{d3}-band at 27 eV. The EELS observations are in accord with the TEM microstructural investigations.

Figure 6a shows the enlarged TEM micrograph, the structure image, of a typical large diamond grain in interface region of

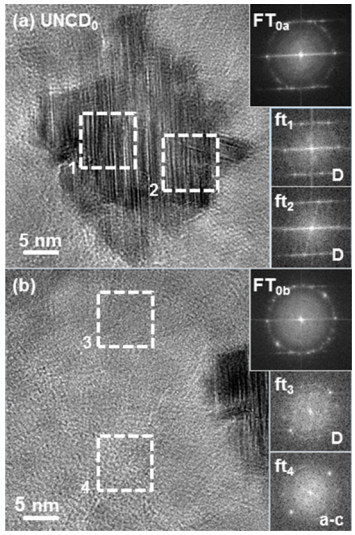

Figure 6. TEM structure image of (a) area I and (b) area II of the interface region of $UNCD_0$ films designated in Figure 4(b_I), respectively. FT_{0a} and FT_{0b} show the Fourier-transformed diffractogram corresponding to the whole structure images in (a) and (b), respectively, whereas the ft_1−ft_4 shows the FT images corresponding to areas 1−4, respectively.

$UNCD_0$ films, which is designated as region I in Figure 4b_I. This micrograph reveals that the large diamond grains are actually the agglomeration of ultrasmall diamond grains. Presumably, the diamond aggregates must have been formed by a coalescence process.[28] Moreover, the coalescence process for forming the diamond aggregates rotated the orientation of the ultrasmall diamond grains into more or less the same orientation, such that the diamond aggregates look like a single crystalline diamond grain, which is indicated by the Fourier-transformed diffractogram (FT_{0a}-image, inset of Figure 6a). Each of the areas contain parallel fringes, implying the presence of planar defects, most probably the stacking faults, which are also implied by the presence of rel-rods associated with the major diffraction spots in ft_1 and ft_2 images corresponding to areas 1 and 2 in Figure 6a. Figure 6b shows the TEM structure image of the region adjacent to the large diamond aggregates (designated as region II, Figure 4b_I). There exist numerous ultrasmall diamond grains in this region, which are implied by the presence of diffraction spots arranged in a ring in the FT_{0b}-image corresponding to entire TEM structure image in Figure 6b. Moreover, the presence of a central diffuse ring in the FT_{0b}-image indicates the existence of abundant sp^2-bonded carbon in these films, which are highlighted by ft_3 and ft_4 images corresponding to areas 3 and 4 in Figure 6b. Notably, the granular structure of UNCD pristine films is uniform throughout the thickness of the films.

DOI: 10.1021/acsami.5b06074
ACS Appl. Mater. Interfaces 2015, 7, 21844−21851

Post-treatment process in $CH_4/Ar/H_2$ plasma (with −300 V bias) markedly alters the microstructure of the UNCD films. Figure 7a_I shows the TEM (BF) micrographs of the surface

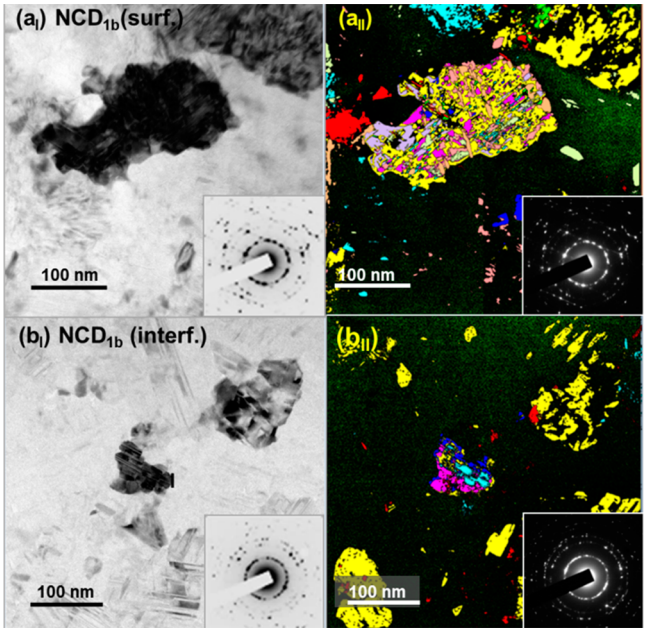

Figure 7. (a_I, b_I) Bright field and (a_{II}, b_{II}) composed dark field TEM micrographs of 30 min plasma post-treated NCD_{1b} films, where (a_I, a_{II}) is for the surface region and (b_I, b_{II}) is for the interface region of the films. The inset shows the corresponding selected area diffraction patterns.

region for 30 min post-treated sample (NCD_{1b}). It shows that the post-treatment process induced marked growth of the diamond aggregates in the surface region of the films to a size as large as hundreds of nanometer. The SAED in the inset of Figure 7a_I contains discrete diffraction spots arranged in a ring shape, which again indicates that most of the diamond grains are large. Presumably, the large diamond grains are formed by the coalescence of the ultrasmall diamond grains. Again, the granular structure of these films is better illustrated by the c-DF TEM image (Figure 7a_{II}). Figure 7a_{II} indicates that there exist some uncoalesced ultrasmall diamond grains besides the large diamond aggregates, implying that the recrystallization process has not been completed in such a short-time plasma post-treatment process. Figure 7, parts b_I and b_{II}, shows the BF and c-DF TEM micrographs of the interface region of the NCD_{1b} sample, respectively. It is surprising to observe that this region of NCD_{1b} sample still contains small diamond aggregates about 80 nm in size, which is about the same size as those in $UNCD_0$ films (cf. Figure 4a). This implies that the granular structure of the interface region of NCD_{1b} samples did not get altered. These observations indicate that the $CH_4/Ar/H_2$ plasma post-treatment process alters the granular structure via a diffusion process. The coalescence process occurs only in the surface layer of the films, where the species in the plasma can be reach (via diffusion). The species in the plasma have not diffused far enough to react with the materials in the interface layer when the sample was post-treated for too short period, and so it remains intact.

Apparently, a longer post-treatment process is required to fully recrystallize the UNCD films. Figures 8a and 9a show the TEM (BF) image of the surface and interface regions of the 60

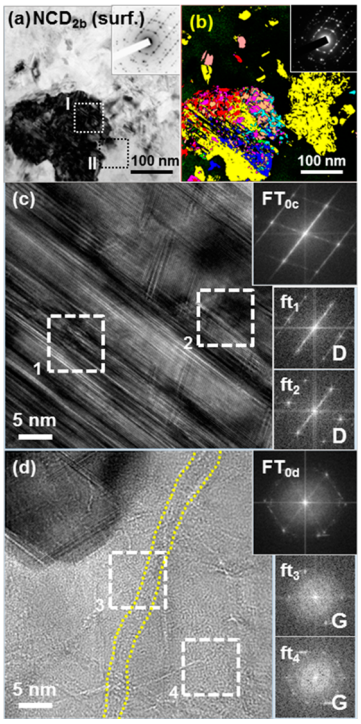

Figure 8. (a) Bright field and (b) composed dark field TEM micrograph of the surface region of NCD_{2b} films, which were plasma post-treated for 60 min. (c) and (d) TEM structure image of the areas I and II in surface region of NCD_{2b} films, respectively (designated in (a)). FT_{0c} and FT_{0d} show the Fourier-transformed diffractogram corresponding to the entire structure images in (c) and (d), respectively, whereas the ft_1−ft_4 shows the FT images corresponding to areas 1−4, respectively.

min $CH_4/Ar/H_2$ plasma post-treated NCD_{2b} films, respectively. These micrographs reveal that the diamond aggregates in both the surface and interface regions increased markedly to a size as large as ∼250 nm, which is about 2−3 times as large as those in UNCD films. The phase constituents of this material are best demonstrated by the c-DF TEM micrograph shown in Figures 8b and 9b, respectively. These micrographs reveal that the region adjacent to a large diamond aggregate (such as region I) is actually another diamond aggregate (e.g., region II). The boundary between the aggregates is rather sharp, like that of the typical NCD films. Moreover, Figures 8c and 9c show the TEM structure image corresponding to typical region of large diamond aggregates (region "I" in Figures 8a and 9a, respectively), which indicates that not only does the size of the diamond aggregates increase, but also the crystallinity of the aggregates improves. The boundaries between the ultrasmall diamond grains disappear such that the whole diamond aggregate looks like a single crystalline diamond grain. However, there are still large amounts of planar defects, stacking faults, and hexagonal diamond clusters, which are implied by the rel-rods associated with major diffraction spots and the systematic row of diffraction spot in FT_{oc} image (insets, Figures 8c and 9c). The presence of stacking faults and hexagonal diamond clusters are further confirmed by the ft_1-image and ft_2-image corresponding to areas 1 and 2 in Figures 8c and 9c, respectively. Notably, the presence of planar defects is the evidence that the coalescence of nanosized diamond grains has occurred during the plasma post-treatment process.[28]

DOI: 10.1021/acsami.5b06074
ACS Appl. Mater. Interfaces 2015, 7, 21844−21851

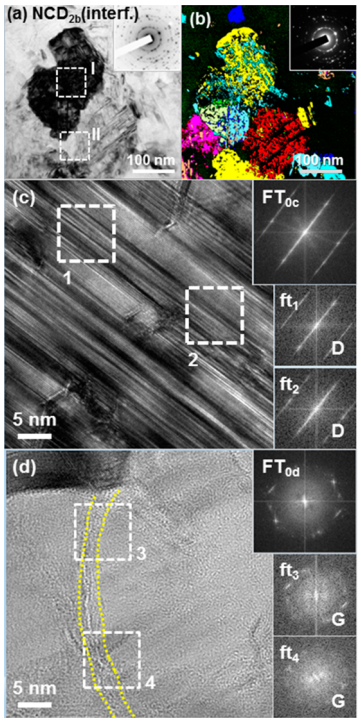

Figure 9. (a) Bright field and (b) composed dark field TEM micrograph of the interface region of NCD_{2b} films, which were plasma post-treated for 60 min. (c) and (d) TEM structure image of the areas I and II in interface region of NCD_{2b} films, respectively (designated in "a"). FT_{0c} and FT_{0d} show the Fourier-transformed diffractogram corresponding to entire structure images in "c" and "d", respectively, whereas the ft_1–ft_4 shows the FT images corresponding to areas 1–4, respectively.

Figures 8d and 9d show the TEM structure images corresponding to the region adjacent to the large diamond aggregates (designated as region II, Figures 8a and 9a). This region is actually another large diamond aggregate, which is oriented away from the zone-axis, weakly diffracting electron, such that the phases in the background shows up. These phases are actually the materials that exist in the boundary between the diamond aggregates. Moreover, these illustrations reveal that, in the grain boundary regions, there appears to be a large number of nanographitic clusters, which are illustrated by the donut-shaped diffraction pattern in FT_{od} images in the inset of Figures 8d and 9d and are highlighted by the ft_3 and ft_4 images corresponding to areas 3 and 4, respectively. Interestingly, sometimes the nanographitic clusters are so densely populated that they form an interconnected path, which is highlighted by a pair of dotted lines in Figures 8d and 9d. Such a high conductivity interconnected channel is presumably the prime factor, which resulted in superior EFE properties of the NCD_{2b} materials (cf. Table 1) compared with the NCD_{1b} materials. Restated, the nanographitic clusters always occur along with the coalescence process of formation of diamond aggregate. It is interesting to observe that not only the surface region, but also the interface region of the NCD_{2b} films undergo microstructural changes, when the UNCD films were post-treated in $CH_4/Ar/H_2$ plasma for long enough periods.

The selected area EELS spectra of the surface and interface regions of NCD_{2b} films are shown as curves II and III in Figure 5, parts a and b, for core-loss and plasmon-loss EELs spectra, respectively. Curves II and III of Figure 5a show that the core-loss EELS spectra of the 60 min plasma post-treated NCD_{2b} films also contain an abrupt rise near 289.5 eV (σ^*-band) and a deep valley near 302 eV, inferring that these materials are predominately diamond. There is an insignificantly small proportion of sp^2-bonded carbon. Moreover, curves II and III of Figure 5b indicate that the plasmon-loss EELS spectra of NCD_{2b} films exhibit a resonant peak at 33 eV (ω_{d4}-band) with a shoulder at 23 eV (ω_{d2}-band), which is the characteristic spectrum of diamond materials. However, the peak intensity ratio, ω_{d2}/ω_{d4}, is slightly larger than $1/\sqrt{2}$, implying that the plasma post-treated NCD_{2b} films contain some amount of amorphous carbon. The EELS observations concur well with the TEM microstructural investigations in Figures 8 and 9.

It should be noted that the NCD films grown directly on Si substrate using $CH_4/Ar/H_2$ plasma also contain uniform diamond grains about 200–300 nm in size. But these films are basically insulating and possess inferior EFE properties, since they contain very sharp and clean grain boundaries. In contrast, the NCD films formed by the modification of the microstructure of UNCD films contain a nanographitic phase along the grain boundaries, which is the prime factor, resulting in enhanced EFE properties of the films. However, the question that remains unsolved is how the plasma post-treatment process alters the granular structure of the UNCD films. To explore the genuine mechanism behind the plasma post-treatment process that modifies the microstructure of the UNCD materials, the constituents of the species contained in the plasma were characterized by optical emission spectroscopy. Spectrum I in Figure 10 shows the OES spectra of CH_4/Ar,

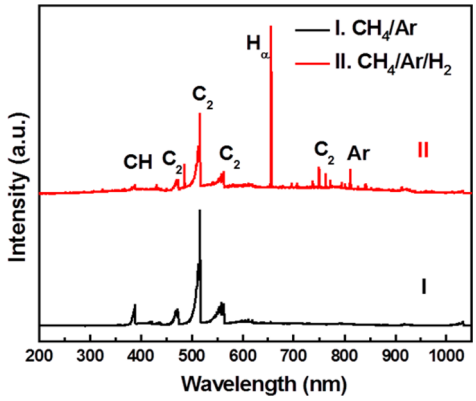

Figure 10. Optical emission spectrum of (I) CH4/Ar plasma used for growing UNCD layers and (II) CH4/Ar/H2 plasma used for the post-treatment of the UNCD layers for growing NCD films.

which were used for growing UNCD films, and spectrum II in Figure 10 reveals the $CH_4/Ar/H_2$ plasma, which were used for the post-treatment process to induce the coalescence of diamond grains. Spectrum I mainly contains a Swan-band with peaks near 470, 512, and 560 nm, which are the emissions from the C_2 species. There also exists a spectral line from CH species near 388 nm.[29,30] The positively charged C_2^+ and CH^+ species are expected to be present in the $CH_4/Ar/H_2$ plasma,[31,32] but the intensities of these spectral lines are too weak to be observable. The spectral lines from Ar species located over the ~700 nm regime are less prominent. Presumably, besides the C_2 species observed in the OES, there are other carbonaceous species, such as C, CH, etc., present in the CH_4/Ar plasma, which do not emit spectral lines. Whether it is the C_2 species that grows UNCD films,[33,34] or the

DOI: 10.1021/acsami.5b06074
ACS Appl. Mater. Interfaces 2015, 7, 21844–21851

other carbonaceous species[35−38] that forms the ultrasmall grain microstructure is still debatable. However, it is clear that the granular structure of UNCD films is very unique, that is, the UNCD films contain uniformly small (∼5 nm) diamond grains. The grain boundary thickness is relatively large (∼0.1 nm). The UNCD films are relatively open in structure compared with NCD or MCD films. Hence, the nanosized diamond grains will coalesce once the encapsulating hydrocarbon layer disintegrates.

In contrast, spectrum II in Figure 10 shows that the$CH_4/Ar/H_2$ plasma contains atomic hydrogen species at 656.3 nm, besides Swan band and Ar species. The presence of atomic hydrogen species is presumed to be the main factor by which the post-treatment processes alter the granular structure of the UNCD layers, as the atomic hydrogen can diffuse almost instantaneously.[39] It is believed that atomic hydrogen present in the plasma first diffused into the UNCD films along the grain boundaries, attacking the hydrocarbon in the grain boundaries and dissociating the tPA phase, which in turn induced the coalescence of the nanosized diamond grains. The C_2 species followed the H species to diffuse inward. The C_2 species were expelled by the coalesced diamond aggregates and finally bonded with one another to form nanographitic phase. These C_2 species are the main ingredients forming the nanographitic phase, which is supported by the observations that when the UNCD films were post-treated in H_2 plasma, coalescence of nanosized diamond grain will occur but formation of nanographitic phase will not be induced.[40] The role of CH species in the plasma on the modification of granular structure of UNCD films is not clear. Probably, it plays the same role as C_2 species in facilitating the formation of nanographitic phase. However, the concentration of CH species is small compared to that of C_2 species, and their effect is expected to be much smaller. The application of bias voltage in the plasma post-treatment process increases the plasma temperature (T_e) and thus increases the amount of C_2 and CH species contained in the plasma relative to H species.[15] Moreover, the application of bias voltage increased the kinetic energy of positive charged species such as C_2^+, CH^+, H^+, Ar^+, etc. However, since the proportion of positive charged species in the plasma is small compared with those of neutral species, the significance of increased kinetic energy for the charged species might not be as important as the increase in proportion of C_2 and CH species.

CONCLUSIONS

Microstructure evolution of diamond films with ultrananocrystalline granular structure as a result of $CH_4/Ar/H_2$ plasma post-treatment processes was investigated. When post-treated for a short period (30 min), only the surface region of diamond films gets coalesced, which converted the ultrasmall diamond grains (∼5 nm) into large diamond aggregates about 200−300 nm in size, whereas the interface region near the diamond-to-Si interface remains intact. The ultrasmall grains rotated to almost align in the same orientation such that the large diamond aggregates look like large single crystalline diamond grains. A large proportion of stacking faults was observed. Only when the diamond films were plasma post-treated for a long enough period (60 min), both the surface and interface regions get recrystallized, resulting in NCD grains (∼hundreds of nanometers) with uniform granular structure. However, a large proportion of nanographitic clusters were induced along the grain boundaries of the films, which resulted in markedly better electron field emission properties of these films, compared with the conventional NCD films grown directly on Si substrates using $CH_4/Ar/H_2$ plasma. OES studies reveal that while the hydrogen species contained in the plasma can induce the coalescence process, the C_2 species is the main ingredient, which induced the formation of a nanographitic phase for facilitating the transport of electrons, thereby improving the EFE properties.

AUTHOR INFORMATION

Corresponding Author

*E-mail: inanlin@mail.tku.edu.tw (I.-N.L.).

Author Contributions

The manuscript was written through contributions of all authors. All authors have given approval to the final version of the manuscript.

Funding

Project No. MOST 103-2112-M-032-002; Ministry of Science and Technology, Republic of China.

Notes

The authors declare no competing financial interest.

ACKNOWLEDGMENTS

The authors are thankful for the financial support of the Ministry of Science and Technology, Republic of China, through Project No. MOST 103-2112-M-032-002.

REFERENCES

(1) Xu, Z.; Bai, X. D.; Wang, E. G.; Wang, Z. L. Field Emission of Individual Carbon Nanotube with *in situ* Tip Image and Real Work Function. *Appl. Phys. Lett.* **2005**, *87*, 163106.

(2) Lu, X.; Yang, Q.; Chen, W.; Xiao, C.; Hirose, A. Field Electron Emission Characteristics of Diamond Films with Different Grain Morphologies. *J. Vac. Sci. Technol.* **2006**, *24*, 2575−2580.

(3) Okano, K.; Koizumi, S.; Silva, S. R. P.; Amaratunga, G. A. J. Low-Threshold Cold Cathodes made of Nitrogen-Doped Chemical-Vapour-Deposited Diamond. *Nature* **1996**, *381*, 140−141.

(4) Sowers, A. T.; Ward, B. L.; English, S. L.; Nemanich, R. J. Field Emission Properties of Nitrogen-doped Diamond Films. *J. Appl. Phys.* **1999**, *86*, 3973−3982.

(5) Geis, M. W.; Efremow, N. N.; Woodhouse, J. D.; Mcaleese, M. D.; Marchywka, M.; Socker, D. G.; Hochedez, J. F. Diamond Cold Cathode. *IEEE Electron Device Lett.* **1991**, *12*, 456−459.

(6) Angus, J. C.; Will, H. A.; Stanko, W. S. Growth of Diamond Seed Crystals by Vapor Deposition. *J. Appl. Phys.* **1968**, *39*, 2915−2922.

(7) Zhou, D.; Krauss, A. R.; Qin, L. C.; McCauley, T. G.; Gruen, D. M.; Corrigan, T. D.; Chang, R. P. H.; Gnaser, H. Synthesis and Electron Field Emission of Nanocrystalline Diamond Thin Films Grown from N_2/CH_4 Microwave Plasmas. *J. Appl. Phys.* **1997**, *82*, 4546−4550.

(8) Catledge, S. A.; Vohra, Y. K. Effect of Nitrogen Addition on the Microstructure and Mechanical Properties of Diamond Films Grown using High-methane Concentrations. *J. Appl. Phys.* **1999**, *86*, 698−700.

(9) Yang, W. B.; Lu, F. X.; Cao, Z. Growth of Nanocrystalline Diamond Protective Coatings on Quartz Glass. *J. Appl. Phys.* **2002**, *91*, 10068−10073.

(10) Stoner, B. R.; Glass, J. T. Textured Diamond Growth on (100) β-SiC via Microwave Plasma Chemical Vapor Deposition. *Appl. Phys. Lett.* **1992**, *60*, 698−700.

(11) Park, J. K.; Lee, W. S.; Baik, Y. J. Grain Size Refinement of the Diamond Film Deposited on the WC−Co Cutting Inserts using Direct Current Biasing. *Surf. Coat. Technol.* **2003**, *171*, 1−5.

(12) Chen, Y. C.; Zhong, X. Y.; Konicek, A. R.; Grierson, D. S.; Tai, N. H.; Lin, I. N.; Kabius, B.; Hiller, J. M.; Sumant, A. V.; Carpick, R. W.; Auciello, O. Synthesis and Characterization of Smooth Ultra-

DOI: 10.1021/acsami.5b06074
ACS Appl. Mater. Interfaces 2015, 7, 21844−21851

nanocrystalline Diamond Films via Low Pressure Bias-enhanced Nucleation and Growth. *Appl. Phys. Lett.* **2008**, *92*, 133113.
(13) Saravanan, A.; Huang, B. R.; Sankaran, K. J.; Dong, C. L.; Tai, N. H.; Lin, I. N. Bias-enhanced Post-treatment Process for Enhancing the Electron Field Emission Properties of Ultrananocrystalline Diamond Films. *Appl. Phys. Lett.* **2015**, *106*, 111602.
(14) Saravanan, A.; Huang, B. R.; Sankaran, K. J.; Kunuku, S.; Dong, C. L.; Leou, K. C.; Tai, N. H.; Lin, I. N. Bias-Enhanced Nucleation and Growth Processes for Ultrananocrystalline Diamond Films in Ar/CH_4 Plasma and Their Enhanced Plasma Illumination Properties. *ACS Appl. Mater. Interfaces* **2014**, *6*, 10566−10575.
(15) Saravanan, A.; Huang, B. R.; Sankaran, K. J.; Keiser, G.; Kurian, J.; Tai, N. H.; Lin, I. N. Structural Modification of Nanocrystalline Diamond Films via Positive/negative Bias Enhanced Nucleation and Growth Processes for Improving their Electron Field Emission Properties. *J. Appl. Phys.* **2015**, *117*, 215307.
(16) Reinke, P.; Kania, P.; Oelhafen, P.; Guggenheim, P. Investigation of the Nucleation Mechanism in Bias-enhanced Diamond Deposition. *Appl. Phys. Lett.* **1996**, *68*, 22−24.
(17) Zhong, X. Y.; Chen, Y. C.; Tai, N. H.; Lin, I. N.; Hiller, J. M.; Auciello, O. Effect of Pretreatment Bias on the Nucleation and Growth Mechanisms of Ultrananocrystalline Diamond Films via Bias-enhanced Nucleation and Growth: An Approach to Interfacial Chemistry Analysis via Chemical Bonding Mapping. *J. Appl. Phys.* **2009**, *105*, 034311.
(18) Teng, K. Y.; Chen, H. C.; Tzeng, G. C.; Tang, C. Y.; Cheng, H. F.; Lin, I. N. Bias-enhanced Nucleation and Growth Processes for Improving the Electron Field Emission Properties of Diamond Films. *J. Appl. Phys.* **2012**, *111*, 053701.
(19) Fowler, R. H.; Nordheim, L. Electron Emission in Intense Electric Fields. *Proc. R. Soc. London, Ser. A* **1928**, *119*, 173−181.
(20) Ferrari, C.; Robertson, J. Resonant Raman Spectroscopy of Disordered, Amorphous and Diamond Like Carbon. *Phys. Rev. B: Condens. Matter Mater. Phys.* **2001**, *64*, 075414.
(21) Ferrari, C.; Robertson, J. Interpretation of Raman Spectra of Disordered and Amorphous Carbon. *Phys. Rev. B: Condens. Matter Mater. Phys.* **2000**, *61*, 14095.
(22) Prawer, S.; Nugent, K. W.; Jamieson, D. N.; Orwa, J. O.; Bursill, L. A.; Peng, J. L. The Raman Spectrum of Nanocrystalline Diamond. *Chem. Phys. Lett.* **2000**, *332*, 93−97.
(23) Filik, J.; Harvey, J. N.; Allan, N. L.; May, P. W. Raman Spectroscopy of Nanocrystalline Diamond: An *ab initio* Approach. *Phys. Rev. B: Condens. Matter Mater. Phys.* **2006**, *74*, 035423.
(24) Gruen, D. M.; Krauss, A. R.; Zuiker, C. D.; Csencsits, R.; Terminello, L. J.; Carlisle, J. A.; Jimenez, I.; Sutherland, D. G. J.; Shuh, D. K.; Tong, W.; Himpsel, F. J. Characterization of Nanocrystalline Diamond Films by Core-level Photoabsorption. *Appl. Phys. Lett.* **1996**, *68*, 1640−1642.
(25) Prawer, S.; Peng, J. L.; Orwa, J. O.; McCallum, J. C.; Jamieson, D. N.; Bursill, L. A. Size Dependence of Structural Stability in Nanocrystalline Diamond. *Phys. Rev. B: Condens. Matter Mater. Phys.* **2000**, *62*, R16360.
(26) Kovarik, P.; Bourdon, E. B. D.; Prince, R. H. Electron-energy-loss Characterization of Laser-deposited a-C, a-C:H and Diamond Films. *Phys. Rev. B: Condens. Matter Mater. Phys.* **1993**, *48*, 12123.
(27) Chen, S. S.; Chen, H. C.; Wang, W. C.; Lee, C. Y.; Lin, I. N. Effects of High Energy Au-ion Irradiation on the Microstructure of Diamond Films. *J. Appl. Phys.* **2013**, *113*, 113704.
(28) Lin, I. N.; Chen, H. C.; Wang, C. S.; Lee, Y. R.; Lee, C. Y. Nanocrystalline Diamond Microstructures from $Ar/H_2/CH_4$-plasma Chemical Vapour Deposition. *CrystEngComm* **2011**, *13*, 6082−6089.
(29) Ivković, M.; Jovićević, S.; Konjević, N. Review: Low Electron Density Diagnostics: Development of Optical Emission Spectroscopic Techniques and Some Applications to Microwave Induced Plasmas. *Spectrochim. Acta, Part B* **2004**, *59*, 591−605.
(30) Yanguas-Gil, A.; Focke, K.; Benedikt, J.; von Keudell, A. Optical and Electrical Characterization of An Atmospheric Pressure Micro-plasma Jet for Ar/CH_4 and Ar/C_2H_2 Mixtures. *J. Appl. Phys.* **2007**, *101*, 103307.
(31) Zhou, D.; Gruen, D. M.; Qin, L. C.; McCauley, T. G.; Krauss, A. R. Control of Diamond Film Microstructure by Ar Additions to CH_4/H_2 Microwave Plasmas. *J. Appl. Phys.* **1998**, *84*, 1981−1989.
(32) Wang, C. S.; Chen, H. C.; Cheng, H. F.; Lin, I. N. Origin of Plate Like Granular Structure for the Ultrananocrystalline Diamond Films Synthesized in H_2-containing Ar/CH_4 Plasma. *J. Appl. Phys.* **2010**, *107*, 034304.
(33) Zhou, D.; McCauley, T. G.; Qin, L. C.; Krauss, A. R.; Gruen, D. M. Synthesis of Nanocrystalline Diamond Thin Films from an $Ar-CH_4$ Microwave Plasma. *J. Appl. Phys.* **1998**, *83*, 540−554.
(34) Gruen, D. M.; Liu, S.; Krauss, A. R.; Pan, X. Buckyball Microwave Plasmas: Fragmentation and Diamond-film Growth. *J. Appl. Phys.* **1994**, *75*, 1758−1763.
(35) May, P. W.; Mankelevich, Y. A. Experiment and Modeling of the Deposition of Ultrananocrystalline Diamond Films using Hot Filament Chemical Vapor Deposition and $Ar/CH_4/H_2$ gas mixtures: A Generalized Mechanism for Ultrananocrystalline Diamond Growth. *J. Appl. Phys.* **2006**, *100*, 024301.
(36) May, P. W.; Mankelevich, Y. A. From Ultrananocrystalline Diamond to Single Crystal Diamond Growth in Hot Filament and Microwave Plasma-Enhanced CVD Reactors: a Unified Model for Growth Rates and Grain Sizes. *J. Phys. Chem. C* **2008**, *112*, 12432−12441.
(37) May, P. W.; Harvey, J. N.; Allan, N. L.; Richley, J. C.; Mankelevich, Y. A. Simulations of Chemical Vapor Deposition Diamond Film Growth using a Kinetic Monte Carlo Model and Two-dimensional Models of Microwave Plasma and Hot Filament Chemical Vapor Deposition Reactors. *J. Appl. Phys.* **2010**, *108*, 114909.
(38) Rodgers, W. J.; May, P. W.; Allan, N. L.; Harvey, J. N. Three-dimensional Kinetic Monte Carlo Simulations of Diamond Chemical Vapor Deposition. *J. Chem. Phys.* **2015**, *142*, 214707.
(39) Joseph, P. T.; Tai, N. H.; Lee, C.-Y.; Niu, H.; Pong, W. F.; Lin, I. N. Field Emission Enhancement in Nitrogen-ion-implanted Ultra-nanocrystalline Diamond Films. *J. Appl. Phys.* **2008**, *103*, 043720.
(40) Sankaran, K. J.; Kunuku, S.; Leou, K. C.; Tai, N. H.; Lin, I. N. Enhancement of the Electron Field Emission Properties of Ultra-nanocrystalline Diamond Films via Hydrogen Post-Treatment. *ACS Appl. Mater. Interfaces* **2014**, *6*, 14543−14551.

DOI: 10.1021/acsami.5b06074
ACS Appl. Mater. Interfaces 2015, 7, 21844−21851